JGR Oceans

RESEARCH ARTICLE
10.1029/2021JC017509

Mechanism of Interannual Cross-Equatorial Overturning Anomalies in the Pacific Ocean

Devanarayana R. M. Rao[1] **and Neil F. Tandon**[1]

[1]Department of Earth and Space Science and Engineering, York University, Toronto, ON, Canada

Key Points:

- Variability of the Pacific meridional overturning circulation is characterized by a prominent cross-equatorial cell (CEC) in the tropics
- The positive phase of the CEC results from a steric equatorially antisymmetric anomaly in sea surface height
- The resulting anomalous northward cross-equatorial flow in the upper Pacific is compensated by anomalous southward flow in the deep Pacific

Supporting Information:

Supporting Information may be found in the online version of this article.

Correspondence to:

D. R. M. Rao,
mdnrao05@gmail.com

Citation:

Rao, D. R. M., & Tandon, N. F. (2021). Mechanism of interannual cross-equatorial overturning anomalies in the Pacific Ocean. *Journal of Geophysical Research: Oceans*, *126*, e2021JC017509. https://doi.org/10.1029/2021JC017509

Received 23 APR 2021
Accepted 27 AUG 2021

Abstract The meridional overturning circulation (MOC) transports heat and mass between the tropics and the extratropics. Recent research has shown that the variability of the Indo-Pacific MOC dominates the variability of the global MOC on interannual timescales, and this variability is characterized by a prominent cross-equatorial cell (CEC) spanning the tropics. This CEC is a potentially important influence on interannual climate variability, but the mechanism responsible for the CEC is not understood. This study seeks to elucidate the mechanism of the CEC using two observational estimates of the ocean. Our analysis shows that the CEC can be explained by the following mechanistic chain: (a) Anomalies in the atmospheric circulation and hydrological cycle produce equatorially antisymmetric density anomalies in the upper Pacific Ocean (above approximately 500 m); (b) these density anomalies generate equatorially antisymmetric anomalies of sea surface height (SSH); (c) these SSH anomalies generate a cross-equatorial flow above approximately 1,000 m; and (d) this anomalous cross-equatorial flow drives compensating flow below approximately 1,000 m. This mechanism contrasts with that responsible for anomalous cross-equatorial overturning on seasonal timescales, which is primarily the Ekman response to equatorially antisymmetric anomalies of zonal wind stress. On interannual timescales, the zonal wind stress anomalies associated with the CEC are equatorially symmetric, and steric SSH variations are the dominant driver of the CEC. These insights may lead to improved understanding and prediction of interannual climate variability.

Plain Language Summary Earth exhibits strong year-to-year variations in climate that have important consequences for economies and livelihoods. Understanding these year-to-year, or "interannual," variations requires understanding variations in the transport of energy by the atmosphere and the ocean. This study focuses on the ocean portion of this transport. Recent research has shown that interannual variations in global ocean transport primarily arise from transport variations in the Indian and Pacific Oceans. Furthermore, this Indo-Pacific variability is characterized by a prominent cross-equatorial cell (CEC) spanning the full depth of the Indian and Pacific Oceans from approximately 18°S to 20°N latitude. We perform an analysis of two ocean models blended with observational data (a standard approach when observational data are sparse) in order to clarify the mechanism responsible for the CEC. Our analysis reveals that the CEC arises because processes in the atmosphere produce changes in upper-ocean density near the equator, which in turn changes the ocean pressure gradient, which in turn drives flow across the equator in the upper ocean and compensating flow in the opposite direction in the deep ocean. Such physical insights may lead to improved understanding and prediction of interannual climate variations.

1. Introduction

The meridional overturning circulation (MOC) plays a significant role in redistributing energy on Earth. This large-scale circulation system transports both heat and mass, and also acts as a source and sink for atmospheric constituents (Talley, 2003). Compared to the atmospheric heat transport, the oceanic meridional heat transport (MHT) dominates in the tropics between 5°S and 15°N (Hartmann, 2016; Held, 2001; Trenberth & Caron, 2001).

The Atlantic MOC (AMOC) has been observed and studied extensively due to its prominent role in the global MOC both in the time average and on multidecadal timescales (e.g., Cunningham et al., 2007; Kuhlbrodt et al., 2007; Marshall & Speer, 2012; Tandon & Kushner, 2015). Much of the past discussion about the global MOC has focused on the physical mechanisms driving the AMOC (e.g., T. Delworth et al., 1993; Jackson

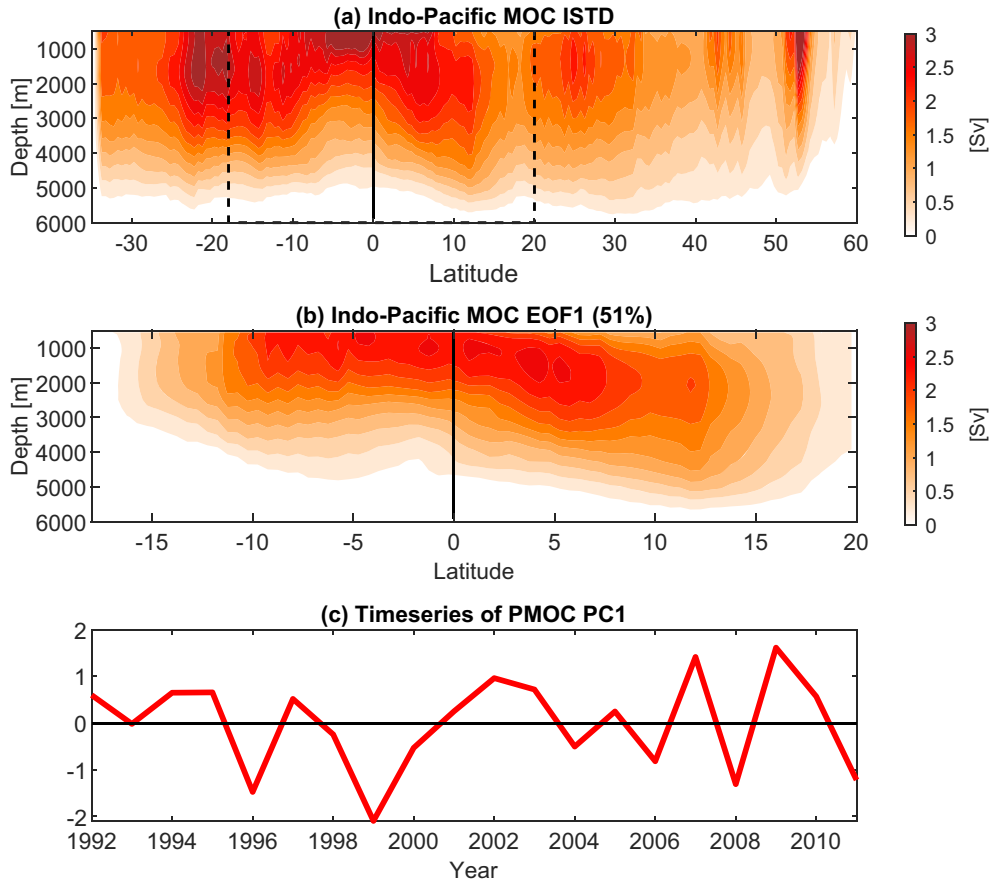

Figure 1. (a) The standard deviation of the annual mean meridional overturning circulation (MOC) stream function for the Indo-Pacific basin calculated from the Estimating the Circulation and Climate of the Ocean (ECCO) state estimate (see Section 2 for details.). The region occupied by the cross-equatorial cell is marked by a dashed box. The shading interval is 0.25 Sv. (b) The ECCO-derived first empirical orthogonal function (EOF) of annual mean Indo-Pacific MOC (PMOC) over the domain 18°S–20°N below 500 m in the Indo-Pacific Ocean. Depths above 500 m have been excluded to focus on variations in deep overturning rather than shallow overturning. The percentage of variance explained by the first EOF is 51%, and the shading interval is 0.25 Sv. (c) The first principal component time series corresponding to the first EOF. We call this first principal component the "PMOC index.".

et al., 2019; Kuhlbrodt et al., 2007). Recent evidence shows that both natural and anthropogenic factors are expected to trigger a slowdown of deep water formation and hence the AMOC (Bryden et al., 2005; IPCC, 2013), with potentially important implications for surface temperature and climate (e.g., Chemke et al., 2020; Hu & Fedorov, 2020).

Compared to the AMOC, the Indo-Pacific MOC (PMOC) has received much less attention. Tandon et al. (2020) have recently shown that interannual PMOC variations span the full depth of the ocean and are especially strong (approximately 3 Sv amplitude; $1\ \text{Sv} = 10^6\ \text{m}^3\ \text{s}^{-1}$) in the tropics (Figure 1a). Furthermore, Tandon et al. (2020) showed that PMOC variations are the dominant driver of interannual oceanic MHT variations, and these variations may interact with the El Niño-Southern Oscillation (ENSO). Therefore, the interannual variability of PMOC is worth investigating because of its potentially important role in climate variability. In this study, we examine the physical mechanism that drives the dominant mode of PMOC variability.

As was shown by Tandon et al. (2020), empirical orthogonal function (EOF) analysis reveals that the most prominent feature of this interannual variability in the deep Indo-Pacific (below ~500 m) is a cross-equatorial cell (CEC) extending from approximately 18°S to 20°N, accounting for more than half of the PMOC variability (Figure 1b). We refer to the associated first principal component (Figure 1c) as the "PMOC index."

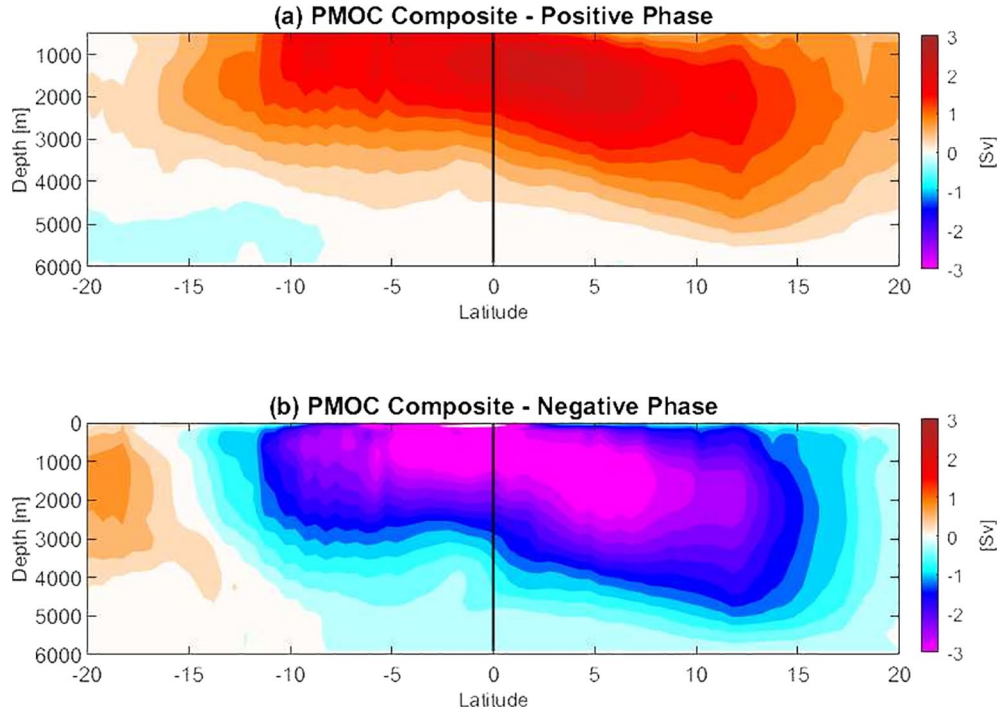

Figure 2. Estimating the Circulation and Climate of the Ocean-derived annual mean Indo-Pacific MOC (PMOC) anomalies averaged over years of (a) PMOC index greater than 0.5 and (b) PMOC index less than – 0.5. The shading interval is 0.25 Sv.

The positive phase of the CEC is shown in Figure 2a, obtained by averaging PMOC anomalies over years during which the PMOC index is greater than 0.5 (1992, 1994, 1995, 1997, 2002, 2003, 2007, 2009, and 2010). When viewed from the east (which we assume hereafter), the positive phase of the CEC indicates anomalous clockwise flow, with anomalous northward flow above approximately 1,000 m and anomalous southward flow below that level. The negative phase of the CEC (Figure 2b, showing PMOC anomalies averaged over years with PMOC index less than – 0.5, that is, 1996, 1999, 2000, 2004, 2006, 2008, and 2011) indicates anomalous counterclockwise flow, with southward flow above ~1,000 m and anomalous northward flow below that level. The positive and negative phases of CEC have a similar structure with the opposite sign, although the negative phase appears to have stronger amplitude with slightly narrower meridional extent compared to the positive phase.

There is also a prominent CEC in the Indo-Pacific on seasonal timescales (Jayne & Marotzke, 2001), driven by equatorially antisymmetric anomalies of zonal wind stress (ZWS). However, such a mechanism does not explain the CEC on interannual timescales, despite the fact that the CEC is ultimately wind-driven (Tandon et al., 2020). Rather, we will show that the CEC is generated by equatorially antisymmetric anomalies of sea surface height (SSH) that result from atmospherically driven density anomalies. (Hereafter, unless otherwise specified, we use "CEC" to refer to the CEC on interannual timescales.)

Section 2 provides additional details on our data and methodology. Section 3 details the roles of wind stresses and SSH variations in driving the anomalous flow above ~1,000 m. The key role of temperature in generating the SSH anomalies is explored. In Section 4, we discuss how atmospheric and oceanic transports generate tropical oceanic heat content anomalies associated with SSH variations. Section 5 provides a summary and concluding remarks.

2. Data and Methods

This study primarily uses the Estimating the Circulation and Climate of the Ocean (ECCO) state estimate version 4, release 2 (Forget et al., 2015, 2016). These data extend from 1992 to 2011 and are interpolated to a $0.5° \times 0.5°$ horizontal grid with 50 vertical levels. ECCO is generated by an ocean model forced by atmospheric fields, which are derived from ERA-Interim reanalysis (Dee et al., 2011). ECCO is also constrained to sea surface temperature (SST) observations from the National Oceanic and Atmospheric Administration (NOAA) (Reynolds et al., 2002), satellite altimetry (Scharroo et al., 2004), the global network of Argo floats (Argo, 2020), and other in-situ and satellite measurements. ECCO outputs all of the necessary fields required to represent the time evolution of the ocean, and it has been previously used for studies of the MOC in the Atlantic and Pacific (e.g., Jackson et al., 2019; Tandon et al., 2020).

In addition to using ECCO, we have also reproduced our key findings (with some notable contrasts) using the Simple Ocean Data Assimilation version 3.12.2 (SODA3) (Carton et al., 2019). (See the Supporting Information S1) SODA3 covers the period from 1980 to 2017, and the ocean model is built on the Geophysical Fluid Dynamics Laboratory Modular Ocean Model version 5 with eddy-permitting $0.25° \times 0.25°$ horizontal resolution and 50 levels (Carton et al., 2018; T. L. Delworth et al., 2012). This particular version of SODA3 is forced by atmospheric fields derived from Japanese 55-year Reanalysis for driving ocean-sea ice models (JRA-55 DO; Tsujino et al., 2018), which is a version of JRA-55 with atmospheric flux corrections. SODA3 assimilates the 2009 World Ocean Database (WOD09) of historical hydrographic profiles (Boyer et al., 2016), in-situ measurements from the International Comprehensive Ocean–Atmosphere Data Set (ICOADS; Woodruff et al., 2011), and SST from NOAA (Reynolds et al., 2007). In contrast with ECCO, SODA3 does not assimilate any velocity information.

In this study, we show computations using the full time range of the SODA3 data set (1980–2017). However, we reach the same conclusions when we confine SODA3 to the same period as ECCO (1992–2011, not shown). As did ECCO, SODA3 produces a CEC that accounts for more than half of the variability in the Indo-Pacific Ocean (Figure S1).

Much of our analysis focuses on the MOC mass stream function, Ψ, that can be expressed in volume units as

$$\Psi(y,z,t) = -\frac{1}{\rho_0}\int_{x_1}^{x_2}\int_{z}^{H}\rho(x,y,z',t)v(x,y,z',t)\,dxdz', \tag{1}$$

where ρ is the density of water, ρ_0 is a constant reference density of water ($\rho_0 = 1029$ kg m^{-3}), v is the meridional velocity in the ocean, x is longitude, y is latitude, z is depth (with corresponding dummy variable z' within the integral), and t is time. We take z to be zero at a reference height for the ocean surface and positive downward. The limits $x_1(y)$ and $x_2(y)$ represent the western and eastern boundaries of the relevant basin at a given latitude, respectively, and $H(x,y)$ is the depth of the ocean bottom at point (x,y). Positive values of Ψ indicate clockwise motion and negative values indicate counterclockwise motion in the depth-latitude plane.

The ocean models in both ECCO and SODA3 apply the Boussinesq approximation. Under this approximation, the contribution of density variations to the mass continuity equation becomes negligible, and Equation 1 reduces to

$$\Psi(y,z,t) = -\int_{x_1}^{x_2}\int_{z}^{H}v(x,y,z',t)dxdz'. \tag{2}$$

In our calculations, v is obtained from ECCO variable "NVELMASS" and SODA3 variable "v," each of which is the resolved northward ocean velocity. As found in Tandon et al. (2020), our results are not sensitive to the inclusion or exclusion of parameterized bolus velocity associated with turbulent transport (Dukowicz & Greatbatch, 1999).

Climate models typically combine the Indian and Pacific Oceans together when computing the MOC stream function (Tandon et al., 2020). Therefore, in order to facilitate a comparison with other studies using climate models and observations, we compute Ψ over the Indo-Pacific. To assess the effect of this choice, Figure 3 shows the ISTD and first EOF of the MOC stream function in the Pacific Ocean, without including the Indian Ocean. Excluding the Indian Ocean results in MOC variability that is approximately 0.5 Sv lower in the Southern Hemisphere (SH, Figure 3a). Figure 3b shows a clear CEC, although the variability is less symmetric about the equator, with notably weaker SH variability compared to the Indo-Pacific CEC. Thus,

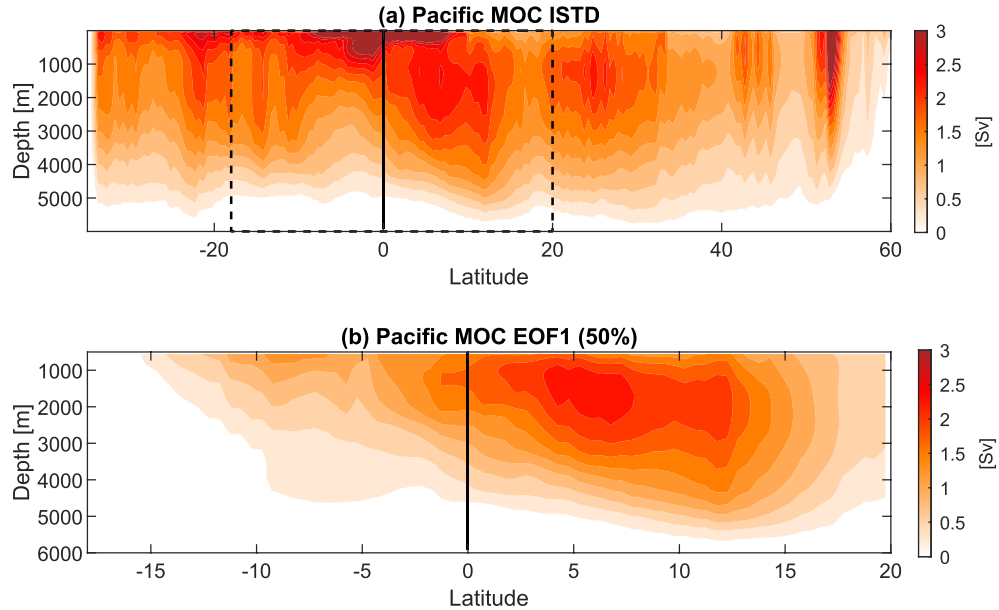

Figure 3. As in Figures 1a and 1b but for the Pacific Ocean, not including the Indian Ocean.

the CEC that is our focus is clearly present whether the Pacific Ocean is examined by itself or in combination with the Indian Ocean.

3. What Drives the Upper Branch of the CEC?

We first consider the possible roles of the zonal and meridional wind stresses in driving the upper branch of the CEC (i.e., the flow above ~1,000 m). The ECCO-derived linear regression onto the PMOC index of the annual mean of the zonally averaged ZWS (blue line in Figure 4a) reveals that, for the positive (clockwise) phase of the CEC, the ZWS anomalies are positive (eastward) at most latitudes within the domain of the CEC. On its own, this anomalous ZWS would drive anomalous northward Ekman transport in SH and southward Ekman transport in the Northern Hemisphere (NH). In other words, this anomalous ZWS would lead to anomalously convergent near-surface flow near the equator, rather than cross-equatorial flow as in the upper branch of the CEC. Hence, Ekman transport due to ZWS anomalies can be ruled out as a direct driver of the CEC. However, ZWS anomalies may play an indirect role, such as through advection of heat in the atmosphere (which we consider further below). Furthermore, the statistical significance of ZWS anomalies south of the equator (and the lack of statistical significance north of the equator) suggests that ZWS-driven Ekman transport may contribute to northward flow in the SH upper branch of the CEC during its positive phase. Here and elsewhere in this study, we determine statistical significance of a linear regression coefficient by computing the p value based on an F-test as implemented in MATLAB's "regress" function.

Approximately 15° away from the equator, SODA3 produces negative ZWS anomalies during the positive phase of the CEC (Figure S2), in contrast with ECCO. However, SODA3 produces positive ZWS anomalies across the equator during the positive phase of the CEC, in agreement with ECCO. Thus, both data sets agree that ZWS does not appear to directly drive anomalous cross-equatorial flow in the upper branch of the CEC.

The annual mean meridional wind stress (MWS) anomalies (red lines in Figure 4a for ECCO and Figure S2 for SODA3) show a correspondence with the sign of the climatological mean MWS: for the positive phase of the CEC, there is a strengthening of the meridional component of the trade winds, which are northward in SH and southward in NH. Such anomalies on their own would drive anomalous near-surface convergence at the equator, rather than the cross-equatorial flow in the upper branch of the CEC. This contrast indicates that MWS anomalies cannot be the direct driver of the upper branch of the CEC.

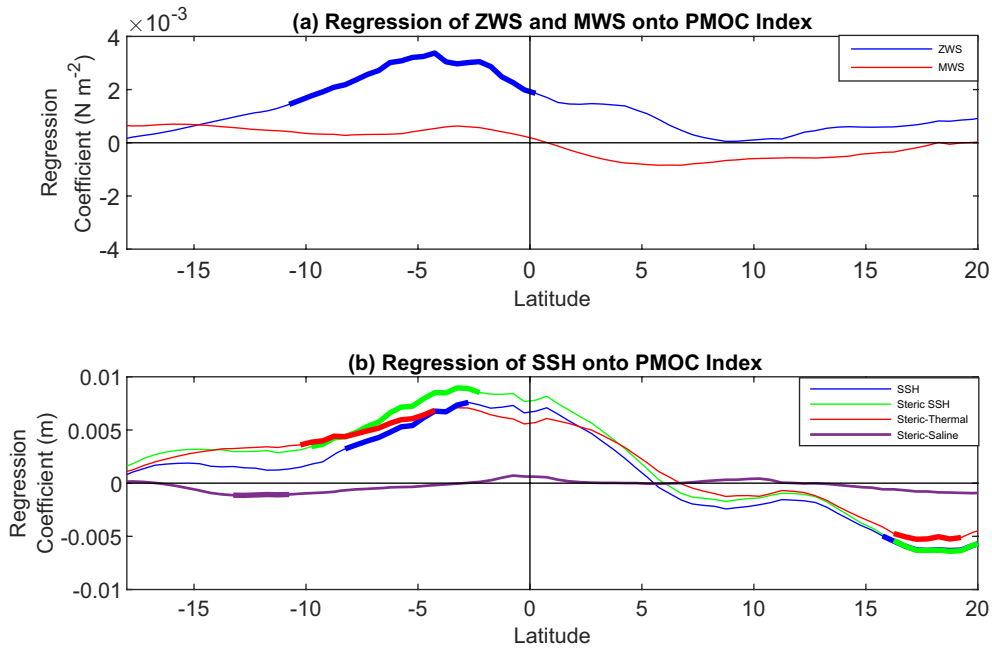

Figure 4. (a)Estimating the Circulation and Climate of the Ocean (ECCO)-derived regressions onto the Indo-Pacific MOC (PMOC) index of annual mean zonally averaged zonal wind stress anomalies (blue) and meridional wind stress anomalies (red). (b) ECCO-derived regressions onto the PMOC index of annual mean zonally averaged sea surface height (SSH) (blue), steric SSH (light green), thermal SSH (red), and saline SSH (purple) anomalies. Thick lines indicate statistically significant values (p values less than or equal to 0.05).

If anomalous wind stresses do not directly drive the near-surface flow in the CEC, what is the mechanism driving the CEC? Anomalies of SSH can provide an explanation, as they can induce a pressure gradient force across the equator. The regression of annual mean SSH anomalies onto the PMOC index is shown in the blue lines in Figure 4b for ECCO and Figure S3 for SODA3. These calculations reveal that, during the positive phase of the CEC, there is an anomalous north-south gradient of SSH, with anomalously high SSH south of the equator and anomalously low SSH north of the equator. Associated with these SSH anomalies is an anomalous northward pressure gradient, which would generate northward flow across the equator.

The role of SSH driving the CEC is further confirmed with a lag correlation between an index of the cross-equatorial SSH gradient (the "SSH seesaw index" or SSI) and the PMOC index (Figure 5 for ECCO and Figure S4 for SODA3). SSI from ECCO is defined as the SSH anomaly averaged over 10°–15°S minus the SSH anomaly over 10°–15°N. In SODA3, the SSI is defined as the SSH anomaly averaged over 15°–20°S minus the

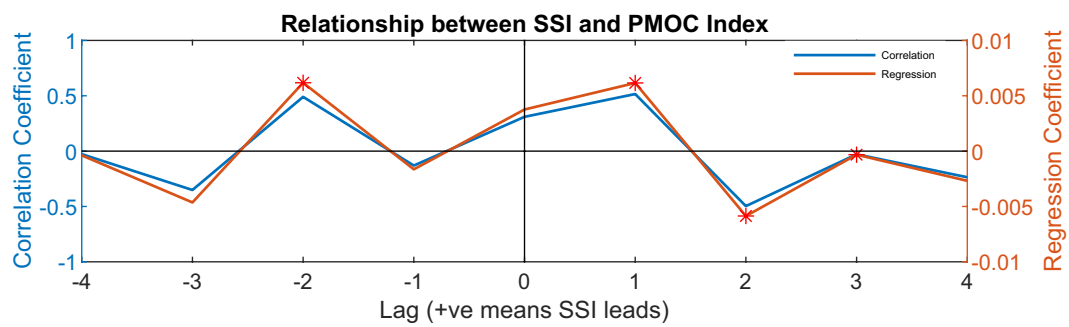

Figure 5. Estimating the Circulation and Climate of the Ocean-derived lag correlation (blue) and lag regression (red) between the annual mean sea surface height seesaw index (SSI) and the Indo-Pacific MOC (PMOC)index. The regression coefficients have units of m. The points that are statistically significant (p value less than or equal to 0.05) are marked with stars. Positive values on the x axis indicate that the SSI is leading the PMOC index.

SSH anomaly over 15°–20°N. The different definitions for the SSI index are meant to capture the latitude ranges where SSH anomalies are strongest and most statistically significant, which are slightly farther from the equator in SODA3 compared to ECCO. SSI is positively correlated with the PMOC index when SSI leads by one year, indicating that a north-south SSH gradient around the equator drives a northward transport in the upper branch of the CEC. Furthermore, as shown by Tandon et al. (2020), anomalous near-surface flow generates a baroclinic response with compensating flow below ~1,000 m. Thus, anomalies of SSH provide a key piece of the mechanism responsible for the CEC.

To what extent are the tropical SSH anomalies driven by density (steric) changes? Steric height changes are produced due to both thermal and saline effects in the water column. The steric height anomaly, η', is computed following Gill and Niller (1973) as

$$\eta' = -\left(\frac{1}{\rho_0}\right)\int_0^H \rho'\, dz \tag{3}$$

with $\rho_0 = 1029$ kg m^{-3}. The annual mean zonal mean steric SSH anomalies computed using Equation 3 in the Indo-Pacific are regressed onto the PMOC index (green lines in Figure 4b for ECCO and Figure S3 for SODA3). These plots show that the structure and magnitude of steric SSH anomalies closely follow the total SSH variations associated with the CEC. This result suggests that the SSH anomalies driving the CEC are indeed generated by density changes rather than dynamical changes.

Are these steric SSH anomalies generated primarily by temperature changes or salinity changes? To address this question, we separate the temperature and salinity contributions to the density anomalies following Vivier et al. (1999). That is,

$$\rho' = \rho_0\left(-\alpha_T\, T' + \beta_S\, S'\right), \tag{4}$$

where T' and S' are anomalies of temperature and salinity, respectively, and α_T and β_S are coefficients of thermal expansion and saline contraction, respectively. Using Equation 4 in Equation 3, we obtain

$$\eta' = \int_0^H \alpha_T\, T' dz - \int_0^H \beta_S\, S' dz. \tag{5}$$

The coefficients are taken to be $\alpha_T = 2\times10^{-4}$ °C^{-1} and $\beta_S = 7.5\times10^{-4}$, approximate average values for the Pacific Ocean.

To isolate the effect of temperature, S' in Equation 5 is set to zero, and the resulting SSH time series is regressed onto the PMOC index (red curves in Figure 4b for ECCO and Figure S3 for SODA3). Conversely, to isolate the effect of salinity, T' in Equation 5 is set to zero, and the resulting SSH time series is regressed onto the PMOC index (purple curves in Figures 4b and S3). In ECCO, the thermal regression closely matches the regression of total density anomalies, whereas the saline regression is relatively flat with respect to latitude. This result suggests that, in ECCO, the SSH anomalies driving the upper branch of the CEC are generated primarily by temperature anomalies.

In SODA3 (Figure S3), SSH anomalies are mostly temperature-driven over approximately 20°S–10°N, and they are mostly salinity-driven between approximately 10°N and 20°N. Despite this contrast with ECCO, the salinity-driven anomalies in SODA3 act to amplify the thermally driven anomalies, and so the overall effect on SSH is similar to that found in ECCO. Figure S5 shows the annual mean sea surface salinity (SSS, shading) and surface current (vectors) regressed onto the PMOC index from SODA3. The SSS anomalies are weakly negative in the eastern Pacific south of about 10°N and in the Indian Ocean south of about 10°S and strongly positive in most other regions. These stronger positive anomalies are responsible for the negative SSH anomalies in the zonal mean (Figure S3).

The current anomalies in Figure S5 do not show any clear correspondence with SSS anomalies. For example, the positive SSS anomaly around 15°N in the eastern Pacific coincides with current anomalies that are overall very weak. These results suggest that the SSS anomalies are likely not driven by ocean advection and are instead driven by changes in precipitation and evaporation. The fact that the SSS increases in the west and north Pacific occur in regions of cooling (not shown) suggests that the SSS increases are likely due to some combination of reduced precipitation and increased wind-driven evaporation, rather than thermally driven increases of evaporation. In other words, the atmosphere, rather than the ocean, appears to drive these SSS anomalies, although additional work is needed to clarify the specific atmospheric processes at

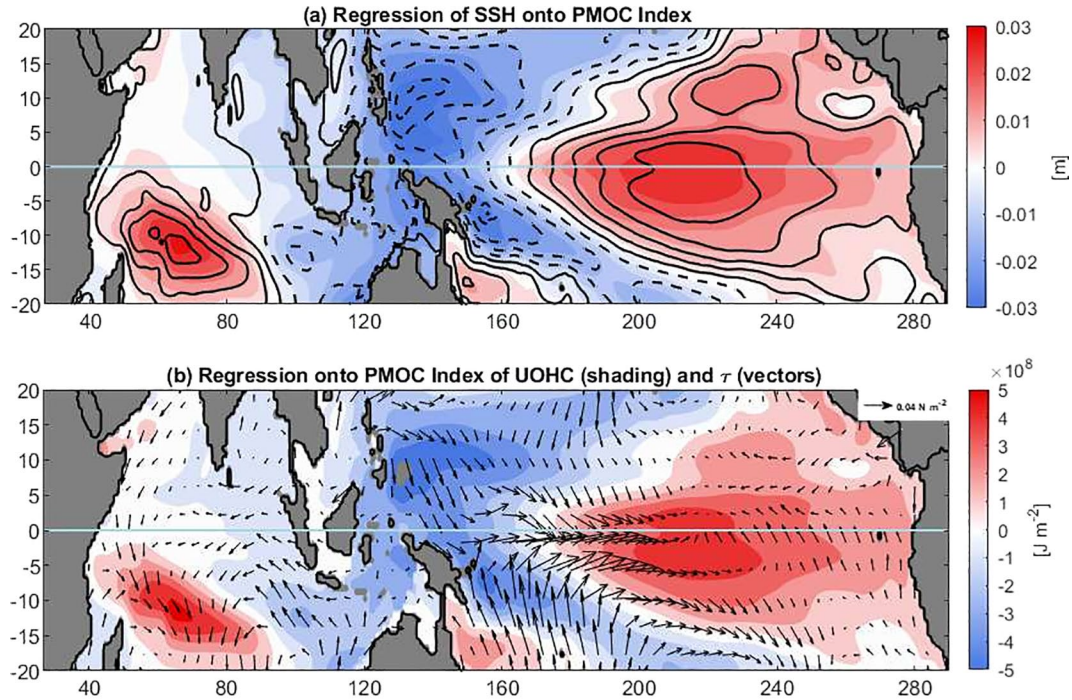

Figure 6. Estimating the Circulation and Climate of the Ocean-derived regressions onto the Indo-Pacific MOC (PMOC) index of (a) annual mean sea surface height (SSH) anomalies (shading), thermal SSH anomalies (contours), (b) upper-ocean heat content anomalies (shading), and wind stress anomalies (vectors). The shading/contour interval in (a) is 4 mm, with negative contours dashed, and the shading interval in (b) is 1×10^8 J m^{-2}.

work. In future studies, it would also be worthwhile to examine additional data sets to assess the combination of temperature and salinity effects on interannual SSH anomalies. In the following section, we focus on ECCO to further understand what generates the temperature anomalies that influence SSH.

4. How are the Thermal SSH Anomalies Generated Near the Equator?

To examine the spatial structure of thermal SSH anomalies in the tropical Indo-Pacific, Figure 6a shows a regression map of annual mean SSH anomalies (shading) and thermal SSH anomalies (contours) onto the PMOC index. Expanding on the zonal mean results of Figures 4b and 6a shows that throughout the tropical Indo-Pacific, the structure and magnitude of the total and thermal SSH anomalies are nearly identical, confirming that the SSH anomalies driving the CEC are thermally generated.

Figure 6a shows that the SSH anomalies are generally positive in the tropical eastern Pacific and negative in the tropical western Pacific. At the equator, the positive SSH anomalies span approximately two-thirds of the basin width and the negative anomalies cover most of the subtropics and extratropics. The equatorial antisymmetry apparent in Figure 4b arises from the fact that the peak of the positive SSH anomalies is south of the equator in the eastern Pacific and the western Indian Ocean, and the peak of the negative SSH anomalies is north of the equator in the western Pacific.

To further examine what is generating these temperature anomalies, the upper-ocean heat content (UOHC) is computed following Zhang et al. (2019) as

$$\mathrm{UOHC} = \rho_0 \mathrm{C_p} \int_0^{H_1} \theta \, dz, \tag{6}$$

where $\mathrm{C_p}$ is the mean specific heat capacity of sea water equal to 3991.86795711963 J kg^{-1} K^{-1}, θ is the potential temperature at 5 m and H_1 = 550 m. Our choice of H_1 aimed to capture the ocean heat content (OHC) above the approximate depth of the tropical thermocline, and our results are not sensitive to the precise choice of H_1. Figure 6b shows annual mean UOHC anomalies (shading) and annual mean wind stress anomalies (vectors) regressed onto the PMOC index. The UOHC anomalies show a structure very similar to

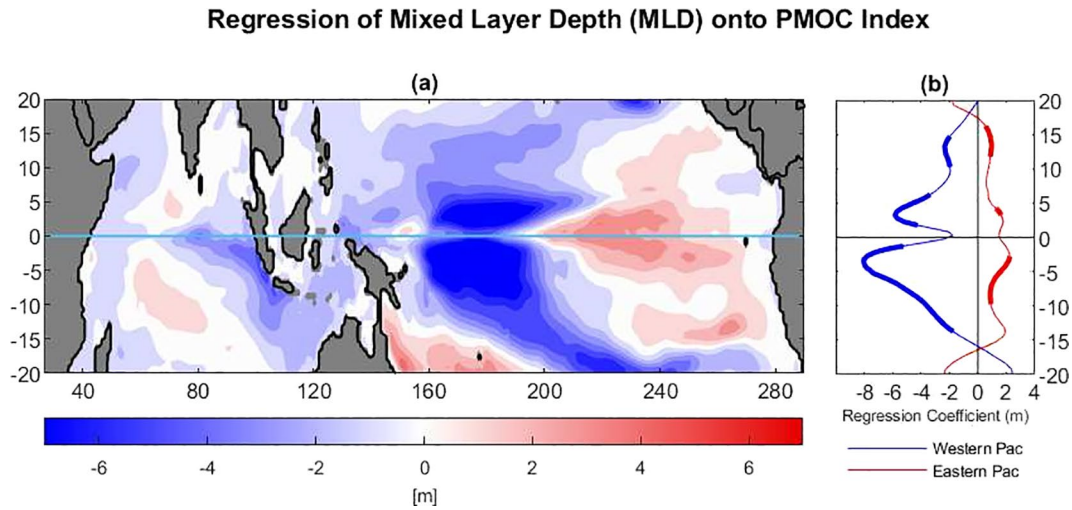

Figure 7. Estimating the Circulation and Climate of the Ocean-derived regression onto the Indo-Pacific MOC (PMOC) index of (a) annual mean mixed layer depth (MLD) and (b) zonal mean of annual mean MLD for the western Pacific (150–210 longitude, blue) and eastern Pacific (240–280 longitude, red). The shading interval in (a) is 1 m. Thick lines in (b) indicate statistically significant points (p value less than or equal to 0.05). Positive values in (b) indicate deepening of the mixed layer.

that of thermal SSH anomalies in Figure 6a. This result suggests that changes in UOHC are responsible for the thermal SSH anomalies near the equator.

To what extent are these UOHC changes reflective of temperature changes at the ocean surface? Indeed, the UOHC anomalies associated with the CEC are qualitatively similar to anomalies of near-surface θ (Figure S6). However, near-surface θ anomalies are nearly symmetric about the equator, in contrast with the equatorially asymmetric UOHC changes. This contrast is especially noticeable in the Indian Ocean, where UOHC anomalies change sign across the equator (Figure 6b), but near-surface θ anomalies are positive on both sides of the equator (Figure S6). We have performed additional calculations (not shown) indicating that the equatorial asymmetry of UOHC anomalies cannot be explained by large-scale vertical velocity anomalies in the ocean. Instead, this asymmetry may be due to the changes in vertical mixing in the upper ocean.

Figure 7 shows the ECCO-derived regression of mixed layer depth (MLD) onto the PMOC index. This plot indicates that in the eastern Pacific and the Indian Ocean, the positive phase of the CEC is associated with MLD deepening that is greater south of the equator than north of the equator. Averaged from the equator to 20° latitude in the eastern Pacific (taken to be 240–280 longitude), the MLD deepening is 0.85 m in SH and 0.73 in NH, which for equatorially symmetric climatological MLD, suggests that surface warming should penetrate more deeply in SH than in NH. This finding may help explain why positive UOHC anomalies in the eastern Pacific and the Indian Ocean peak south of the equator (Figure 6b).

In the western Pacific, the mixed layer shallowing is weaker north of the equator than south of the equator. Averaged from the equator to 20° latitude in the western Pacific (taken to be 150–210 longitude), the MLD change is – 3.0 m in SH and – 2.3 m in NH, which for equatorially symmetric climatological MLD, would imply a deeper mixed layer in NH than in SH. This result may explain why the decrease of UOHC peaks north of the equator (Figure 6b). Further work is needed to confirm this role of MLD and investigate the mechanisms responsible for these MLD variations. We have also examined climatological MLD, but there is no clear equatorial asymmetry in climatological MLD that would explain the equatorial asymmetry in interannual UOHC anomalies (not shown).

The above analysis suggests that tropical UOHC changes associated with the CEC arise primarily from equatorially symmetric changes in near-surface temperature, and the vertical mixing of these near-surface temperature anomalies is spatially uneven, resulting in equatorially asymmetric variations in UOHC. Thus, another key piece of the CEC mechanism requires understanding what generates the near-surface

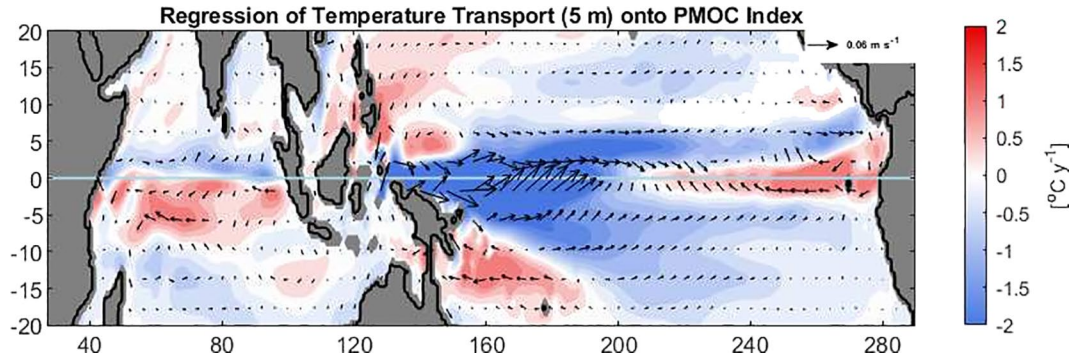

Figure 8. Estimating the Circulation and Climate of the Ocean-derived regression onto the Indo-Pacific MOC (PMOC) index of annual mean temperature transport anomalies (shading) and ocean velocity anomalies at 5 m (vectors). The shading interval is 0.25°C y^{-1}.

temperature anomalies. Anomalies of wind stress (vectors in Figure 6b) are primarily eastward at the equator, which we expect to drive warm water from the western Pacific to the eastern Pacific and suppress upwelling in the eastern Pacific. Such anomalies resemble the weakening of the Walker Circulation and the corresponding warming in the eastern equatorial Pacific that occur under El Niño. The warm anomaly in the southwestern Indian Ocean corresponds with anomalous poleward wind stress, suggesting that the transport of warm water or air from around the equator is responsible for this anomaly. The cool anomalies in the western and subtropical Pacific and in the eastern Indian Ocean correspond with anomalous equatorward wind stress, suggesting that the transport of cooler water or air from higher latitudes is responsible. The SSH anomalies in the Indian Ocean (Figure 6a) resemble the SSH anomalies associated with the Indian Ocean Dipole (IOD) (Deepa et al., 2018), although the negative anomalies associated with CEC are weaker than those associated with the IOD. Deepa et al. (2018) found that the thermal SSH anomalies associated with the IOD are induced by interannual variations in wind stress.

Are the temperature anomalies associated with the CEC due primarily to transport within the ocean or transport within the atmosphere? To address this question, Figure 8 shows a regression map of annual mean surface currents (vectors) onto the PMOC index. The surface current anomalies suggest that wind-driven transport within the ocean may be partially responsible for generating temperature anomalies in the equatorial Pacific. However, away from the equator, the role of the ocean currents appears to be small. Surprisingly, ocean current anomalies in the equatorial east Pacific are directed away from the South American coast, implying anomalous upwelling, in contrast with our expectation of anomalous downwelling associated with warming in this region. This finding highlights a contrast between the positive phase of the CEC and El Niño, during which there is warming in the equatorial east Pacific associated with anomalous downwelling.

To further assess the role of ocean temperature advection, we consider the ocean thermodynamic equation,

$$\frac{\partial \theta}{\partial t} + \mathbf{v} \cdot \nabla \theta = Q, \tag{7}$$

where Q is diabatic heating and $\mathbf{v}$ is the ocean velocity with zonal, meridional, and vertical components (u, v, w). Rearranging Equation 7, we obtain

$$\frac{\partial \theta}{\partial t} = -\mathbf{v} \cdot \nabla \theta + Q = \frac{\partial \theta_{adv}}{\partial t} + Q, \tag{8}$$

where $\partial_t \theta_{adv} \equiv -\mathbf{v} \cdot \nabla \theta$ captures the effect of temperature advection. The effect of time variations in ocean transport on temperature would then be

$$\frac{\partial \theta'_{adv}}{\partial t} = -u' \frac{\partial \bar{\theta}}{\partial x} - v' \frac{\partial \bar{\theta}}{\partial y} - w' \frac{\partial \bar{\theta}}{\partial z}, \tag{9}$$

where overbars indicate time averages and primes indicate deviations from time averages.

The regression of annual mean $\partial_t \theta'_{adv}$ onto the PMOC index is shown in Figure 8 (shading). These anomalies suggest that ocean transport is partially responsible for cooling in the western Pacific and warming in the eastern Pacific. We obtained a nearly identical pattern when we neglected vertical advection (not

shown), suggesting that horizontal surface currents are primarily responsible for this pattern (although vertical advection is expected to play a stronger role at deeper levels). Such a $\partial_t \theta'_{adv}$ pattern is expected, as the anomalous horizontal near-surface current transports water from the relatively warm western Pacific to the relatively cool eastern Pacific. However, the pattern of heating and cooling is very different from those in Figures 8b and S6, suggesting that ocean heat transport is likely not the main driver of the interannual temperature anomalies responsible for driving the CEC.

Altogether, these findings suggest that atmospheric transport combined with changes in ocean vertical mixing play crucial roles in determining the overall pattern of tropical heating and cooling that drive the CEC. The role of atmospheric transport provides an important point of comparison with earlier research. Tandon et al. (2020) performed idealized model experiments revealing that interannual variations in wind stress were primarily responsible for interannual PMOC variations. Our results agree with that finding and further clarify that the influence of these wind stress variations on the CEC is mediated through their generation of tropical temperature anomalies in the upper ocean, which (possibly in combination with salinity anomalies) generate SSH anomalies that drive anomalous cross-equatorial flow. Furthermore, while wind-driven Ekman transport does not appear to play a primary role in driving the CEC, Tandon et al. (2020) showed evidence that it does play a primary role in driving interannual PMOC variability farther away from the equator at latitudes outside of the CEC. Additional work is needed to assess the extent to which atmospheric processes are responsible for changes in vertical mixing that appear to influence the CEC.

5. Conclusion

This study has sought to clarify the mechanism responsible for the CEC, the dominant mode of interannual PMOC variability in the tropics. Our analysis combined with results of earlier research suggests that the mechanism driving the positive phase of the CEC is as follows:

1. On interannual timescales, wind stress anomalies generate anomalies of surface temperature and salinity in the tropics.
2. The vertical mixing of the surface temperature anomalies is spatially uneven, resulting in equatorially antisymmetric anomalies of UOHC.
3. These UOHC and salinity anomalies generate equatorially antisymmetric anomalies of zonal mean SSH, which in turn generate an anomalous north-south pressure gradient across the equator.
4. This anomalous pressure gradient generates a pressure gradient force that drives anomalous northward cross-equatorial flow above approximately 1,000 m in the Pacific Ocean.
5. As the basin undergoes baroclinic adjustment, this anomalous northward flow above ~1,000 m is compensated by a southward flow below ~1,000 m, thereby forming a clockwise overturning circulation cell.

These findings build on the results of Tandon et al. (2020), who found that interannual wind stress anomalies were the primary driver of interannual PMOC variations. Our results help to clarify that the influence of these wind stress variations on the CEC is mediated through their generation of density anomalies that in turn generate SSH anomalies.

As mentioned above, ECCO and SODA3 produce different results regarding the dominance of temperature effects compared to salinity effects on SSH. Interannual SSH variations in ECCO are almost entirely driven by temperature changes, whereas salinity plays an important role in SODA3. ECCO and SODA3 use different atmospheric forcing data sets (ERA-Interim and JRA-55 DO, respectively), which might influence the relative roles of temperature and salinity. This is a matter worth investigating in future studies. Recent studies have shown that internal variability of ocean density has also produced equatorially asymmetric trends of SSH and OHC on decadal timescales (Rathore et al., 2020; Schloesser et al., 2021). However, the associated spin up of the South Pacific subtropical gyre on decadal timescales (Schloesser et al., 2021) is not apparent on interannual timescales (Figure 6b). Rather, our analysis suggests that on interannual timescales, equatorially asymmetric changes in vertical mixing may play a role in generating equatorially asymmetric changes in UOHC. As mentioned above, the mechanisms responsible for this asymmetry in anomalous vertical mixing require further investigation.

There is an intriguing similarity between the temperature anomalies associated with the positive phase of the CEC and those associated with the positive phase of ENSO. The lag correlation analysis of Tandon et al. (2020) showed that ENSO and PMOC are correlated, but the correlation is not especially high; in ECCO, the simultaneous correlation between the PMOC index and a standard ENSO index is less than 0.5. This result points to possible interaction between PMOC and ENSO, rather than the PMOC simply being an alternative index of ENSO. Such interaction is an important topic to explore in future studies, given the potential importance to ENSO prediction. In the Indian Ocean, as mentioned earlier, there is a similarity between the SSH anomalies associated with the CEC and SSH anomalies associated with the IOD (Deepa et al., 2018) and the Pacific Decadal Oscillation (PDO) (Deepa et al., 2019). Thus, in future studies, it would also be worthwhile to explore the possible interaction between the CEC and these other modes of climate variability.

Data Availability Statement

The ECCO state estimate used for this study is publicly available from the NASA Earthdata archive (https://ecco.jpl.nasa.gov/drive/). The SODA3 data are available from the data repository of the National Center for Atmospheric Research (https://rda.ucar.edu/datasets/ds650.0/).

Acknowledgments
This research was funded in part by a Discovery Grant from the Natural Sciences and Engineering Research Council of Canada (NSERC). The authors are grateful to Oleg Saenko, Kaz Higuchi, Peter Taylor, Gary Klaassen, Thabo Mpanza, and Noah Stanton for constructive comments on an earlier version of the manuscript. Two anonymous reviewers provided valuable feedback on the submitted manuscript.

References

Argo. (2020). *Argo float data and metadata from Global Data Assembly Centre*. Argo GDAC. [Dataset]. https://doi.org/10.17882/42182

Boyer, T., Domingues, C. M., Good, S. A., Johnson, G. C., Lyman, J. M., Ishii, M., et al. (2016). Sensitivity of global upper-ocean heat content estimates to mapping methods, XBT bias corrections, and baseline climatologies. *Journal of Climate*, *29*(13), 4817–4842. https://doi.org/10.1175/JCLI-D-15-0801.1

Bryden, H. L., Longworth, H. R., & Cunningham, S. A. (2005). Slowing of the Atlantic meridional overturning circulation at 25°N. *Nature*, *438*(7068), 655–657. https://doi.org/10.1038/nature04385

Carton, J. A., Chepurin, G. A., Chen, L., Grodsky, S., Kalnay, E., & Penny, S. G. (2019). *SODA Project: SODA3 ensemble means and standard deviations*: Research Data Archive at the National Center for Atmospheric Research, Computational and Information Systems Laboratory. https://doi.org/10.5065/HBTB-R521

Carton, J. A., Chepurin, G. A., Chen, L., & Grodsky, S. A. (2018). Improved global net surface heat flux. *Journal of Geophysical Research: Oceans*, *123*(5), 3144–3163. https://doi.org/10.1002/2017JC013137

Chemke, R., Zanna, L., & Polvani, L. M. (2020). Identifying a human signal in the North Atlantic warming hole. *Nature Communications*, *11*(1), 1540. https://doi.org/10.1038/s41467-020-15285-x

Cunningham, S. A., Kanzow, T., Rayner, D., Baringer, M. O., Johns, W. E., Marotzke, J., et al. (2007). Temporal variability of the Atlantic meridional overturning circulation at 26.5°N. *Science*, *317*(5840), 935–938. https://doi.org/10.1126/science.1141304

Dee, D. P., Uppala, S. M., Simmons, A. J., Berrisford, P., Poli, P., Kobayashi, S., et al. (2011). The ERA-Interim reanalysis: Configuration and performance of the data assimilation system. *Quarterly Journal of the Royal Meteorological Society*, *137*(656), 553–597. https://doi.org/10.1002/qj.828

Deepa, J. S., Gnanaseelan, C., Kakatkar, R., Parekh, A., & Chowdary, J. S. (2018). The interannual sea level variability in the indian ocean as simulated by an ocean general circulation model. *International Journal of Climatology*, *38*(3), 1132–1144. https://doi.org/10.1002/joc.5228

Deepa, J. S., Gnanaseelan, C., Mohapatra, S., Chowdary, J. S., Karmakar, A., Kakatkar, R., & Parekh, A. (2019). The Tropical Indian Ocean decadal sea level response to the Pacific Decadal Oscillation forcing. *Climate Dynamics*, *52*(7), 5045–5058. https://doi.org/10.1007/s00382-018-4431-9

Delworth, T., Manabe, S., & Stouffer, R. J. (1993). Interdecadal variations of the thermohaline circulation in a coupled ocean-atmosphere model. *Journal of Climate*, *6*, 1993–2011. https://doi.org/10.1175/1520-0442(1993)006<1993:IVOTTC>2.0.CO;2

Delworth, T. L., Rosati, A., Anderson, W., Adcroft, A. J., Balaji, V., Benson, R., et al. (2012). Simulated climate and climate change in the GFDL CM2.5 high-resolution coupled climate model. *Journal of Climate*, *25*(8), 2755–2781. https://doi.org/10.1175/JCLI-D-11-00316.1

Dukowicz, J. K., & Greatbatch, R. J. (1999). The bolus velocity in the stochastic theory of ocean turbulent tracer transport. *Journal of Physical Oceanography*, *29*(9), 2232–2239. https://doi.org/10.1175/1520-0485(1999)029<2232:TBVITS>2.0.CO;2

Forget, G., Campin, J.-M., Heimbach, C. N., Hill, P., Ponte, R. M., & Wunsch, C. (2016). *ECCO version 4: Second release*. MIT Libraries DSpace@MIT, Retrieved from http://hdl.handle.net/1721.1/102062

Forget, G., Campin, J.-M., Heimbach, P., Hill, C. N., Ponte, R. M., & Wunsch, C. (2015). ECCO version 4: An integrated framework for non-linear inverse modeling and global ocean state estimation. *Geoscientific Model Development*, *8*(10), 3071–3104. https://doi.org/10.5194/gmd-8-3071-2015

Gill, A., & Niller, P. (1973). The theory of the seasonal variability in the ocean. *Deep-Sea Research and Oceanographic Abstracts*, *20*(2), 141–177. https://doi.org/10.1016/0011-7471(73)90049-1

Hartmann, D. L. (Ed.). (2016). *Global physical climatology* (Second Edition). Elsevier. https://doi.org/10.1016/B978-0-12-328531-7.00002-5

Held, I. M. (2001). The partitioning of the poleward energy transport between the Tropical Ocean and atmosphere. *Journal of the Atmospheric Sciences*, *58*(8), 943–948. https://doi.org/10.1175/1520-0469(2001)058<0943:TPOTPE>2.0.CO;2

Hu, S., & Fedorov, A. V. (2020). Indian Ocean warming as a driver of the North Atlantic warming hole. *Nature Communications*, *11*(1), 4785. https://doi.org/10.1038/s41467-020-18522-5

IPCC. (2013). Summary for policymakers [Book Section], In T. Stocker (Ed.), In *Climate change 2013: The physical science basis. contribution of working group I to the fifth assessment report of the Intergovernmental Panel on Climate Change*. 1–30: Cambridge University Press. https://doi.org/10.1017/CBO9781107415324.004

Jackson, L. C., Dubois, C., Forget, G., Haines, K., Harrison, M., Iovino, D., et al. (2019). The mean state and variability of the North Atlantic circulation: A perspective from ocean reanalyses. *Journal of Geophysical Research: Oceans*, *124*(12), 9141–9170. https://doi.org/10.1029/2019JC015210

Jayne, S. R., & Marotzke, J. (2001). The dynamics of ocean heat transport variability. *Reviews of Geophysics*, *39*(3), 385–411. https://doi.org/10.1029/2000RG000084

Kuhlbrodt, T., Griesel, A., Montoya, M., Levermann, A., Hofmann, M., & Rahmstorf, S. (2007). On the driving processes of the Atlantic meridional overturning circulation. *Reviews of Geophysics*, *45*(2), RG2001. https://doi.org/10.1029/2004RG000166

Marshall, J., & Speer, K. (2012). Closure of the meridional overturning circulation through Southern Ocean upwelling. *Nature Geoscience*, *5*(3), 171–180. https://doi.org/10.1038/ngeo1391

Rathore, S., Bindoff, N. L., Phillips, H. E., & Feng, M. (2020). Recent hemispheric asymmetry in global ocean warming induced by climate change and internal variability. *Nature Communications*, *11*(1). https://doi.org/10.1038/s41467-020-15754-3

Reynolds, R. W., Rayner, N. A., Smith, T. M., Stokes, D. C., & Wang, W. (2002). An improved in situ and satellite SST analysis for climate. *Journal of Climate*, *15*(13), 1609–1625. https://doi.org/10.1175/1520-0442(2002)015<1609:AIISAS>2.0.CO;2

Reynolds, R. W., Smith, T. M., Liu, C., Chelton, D. B., Casey, K. S., & Schlax, M. G. (2007). Daily high-resolution-blended analyses for sea surface temperature. *Journal of Climate*, *20*(22), 5473–5496. https://doi.org/10.1175/2007JCLI1824.1

Scharroo, R., Lillibridge, J. L., Smith, W. H. F., & Schrama, E. J. O. (2004). Cross-calibration and long-term monitoring of the microwave radiometers of ERS, TOPEX, GFO, Jason, and Envisat. *Marine Geodesy*, *27*(1–2), 279–297. https://doi.org/10.1080/01490410490465265

Schloesser, F., Thompson, P. R., & Piecuch, C. G. (2021). Meridional asymmetry in recent decadal sea-level trends in the subtropical Pacific Ocean. *Geophysical Research Letters*, *48*(6), e2020GL091959. https://doi.org/10.1029/2020GL091959

Talley, L. D. (2003). Shallow, intermediate, and deep overturning components of the global heat budget. *Journal of Physical Oceanography*, *33*(3), 530–560. https://doi.org/10.1175/1520-0485(2003)033<0530:SIADOC>2.0.CO;2

Tandon, N. F., & Kushner, P. J. (2015). Does external forcing interfere with the AMOC's influence on North Atlantic sea surface temperature? *Journal of Climate*, *28*(16), 6309–6323. https://doi.org/10.1175/JCLI-D-14-00664.1

Tandon, N. F., Saenko, O. A., Cane, M. A., & Kushner, P. J. (2020). Interannual variability of the global meridional overturning circulation dominated by Pacific variability. *Journal of Physical Oceanography*, *50*(3), 559–574. https://doi.org/10.1175/JPO-D-19-0129.1

Trenberth, K. E., & Caron, J. M. (2001). Estimates of meridional atmosphere and ocean heat transports. *Journal of Climate*, *14*(16), 3433–3443. https://doi.org/10.1175/1520-0442(2001)014<3433:EOMAAO>2.0.CO;2

Tsujino, H., Urakawa, S., Nakano, H., Small, R. J., Kim, W. M., Yeager, S. G., et al. (2018). JRA-55 based surface dataset for driving ocean–sea-ice models (JRA55-do). *Ocean Modelling*, *130*, 79–139. https://doi.org/10.1016/j.ocemod.2018.07.002

Vivier, F., Kelly, K. A., & Thompson, L. (1999). Contributions of wind forcing, waves, and surface heating to sea surface height observations in the Pacific Ocean. *Journal of Geophysical Research*, *104*(C9), 20767–20788. https://doi.org/10.1029/1999JC900096

Woodruff, S. D., Worley, S. J., Lubker, S. J., Ji, Z., Eric Freeman, J., Berry, D. I., et al. (2011). ICOADS Release 2.5: Extensions and enhancements to the surface marine meteorological archive. *International Journal of Climatology*, *31*(7), 951–967. https://doi.org/10.1002/joc.2103

Zhang, C., Han, X., & Lin, X. (2019). Quantifying the non-conservative production of potential temperature over the past 22 000 years. *Journal of Oceanology and Limnology*, *37*(2), 410–422. https://doi.org/10.1007/s00343-019-8067-3